Petroleum Science 22 (2025) 2233–2245

KeAi
CHINESE ROOTS
GLOBAL IMPACT

Contents lists available at ScienceDirect

Petroleum Science

journal homepage: www.keaipublishing.com/en/journals/petroleum-science

Original Paper

Molecular dynamics insights into wax formation—How polymeric inhibitors shape crude oil flow

Wyclif Kiyingi [a], Ji-Xiang Guo [a, *], Rui-Ying Xiong [b, c], Chen-Hao Gao [a]

[a] *Unconventional Petroleum Research Institute, China University of Petroleum (Beijing), Beijing, 102249, China*
[b] *College of Petroleum Engineering, China University of Petroleum (Beijing), Beijing, 102249, China*
[c] *State Key Laboratory of Petroleum Resources and Prospecting, China University of Petroleum (Beijing), Beijing, 102249, China*

ARTICLE INFO

Article history:
Received 28 October 2024
Received in revised form
30 December 2024
Accepted 2 March 2025
Available online 4 March 2025

Edited by Min Li

Keywords:
Molecular dynamics
Colloids
Crystal growth
Adsorption energy
Polymeric inhibitor

ABSTRACT

Molecular-level interactions between polymeric inhibitors and wax crystals are essential for mitigating wax deposition in crude oils, a major operational and environmental challenge. This study investigates the mechanisms by which specific inhibitors target wax crystals to prevent aggregation. Extracted wax and inhibitor were characterized using gas chromatography, X-ray diffraction, and spectroscopy to determine the molecular structures. The wax primarily comprised of straight-chain $n\mathrm{C}_{28}$ alkanes, while the inhibitor was an ethylene/vinyl acetate copolymer. Rheological tests demonstrated a reduced gelation point upon inhibitor addition.

Molecular dynamics (MD) simulations, performed using the COMPASS II force field, revealed interactions at the molecular level. Structural validation of molecules was done through comparative analysis of the experimental infrared and simulated vibrational analysis spectra whereas that of the rhombohedral wax crystal was achieved using the Pawley method, yielding a Profile *R*-factor of 9.26%. Morphological studies revealed five symmetrically unique facets, with the (110) plane being the fastest-growing due to its inter-planar distance and attachment energy (−157.25 kcal/mol). Adsorption energy calculations (−180 kcal/mol) confirmed that the inhibitor effectively disrupted crystal growth on the surface by adsorbing its polar section onto the wax surface while repelling the non-polar groups, thereby reducing wax aggregation.

1. Introduction

The exploration and production of crude oil remain crucial to the global energy supply, with the efficiency and sustainability of extraction and transportation processes being key concerns. One of the major operational challenges in oil wells and pipelines is the formation of wax crystals, particularly under low temperature conditions, leading to blockages, reduced flow rates, and increased costs (Elkatory et al., 2022; Kiyingi et al., 2022; Li et al., 2023). This phenomenon is triggered when the temperature of crude oil drops below the wax appearance temperature (WAT), initiating wax crystallization (Haj-Shafiei et al., 2019; Paiva et al., 2017; Taheri-Shakib et al., 2018). The wax crystals, primarily composed of long-chain *n*-alkanes, grow and aggregate, altering the crude oil's rheological properties and posing significant flow assurance challenges. The morphology and size of the crystals directly influence the severity of wax deposition, as highlighted by numerous studies (Haj-Shafiei et al., 2019; Li et al., 2023; Van der Geest et al., 2021). Thus, there is an urgent need to develop effective strategies to mitigate these risks.

One promising approach is the use of polymeric inhibitors to control wax crystal growth. These high-molecular-weight polymers inhibit crystal aggregation, which helps maintain the flow properties of crude oil. Research has demonstrated that the molecular structure and concentration of polymeric inhibitors are critical to their effectiveness in altering the crystallization process (Kiyingi et al., 2022; Li et al., 2021). However, while these studies have provided insights into the general effectiveness of inhibitors, there remains a gap in understanding the molecular-level interactions between the inhibitors and the crude oil wax crystals.

In recent years, molecular dynamics (MD) has emerged as a powerful tool to study the behavior of molecules at the atomic

---

* Corresponding author.
E-mail address: guojx003@126.com (J.-X. Guo).

https://doi.org/10.1016/j.petsci.2025.03.001

scale. MD simulations can provide detailed insights into the kinetic and thermodynamic behavior of complex systems, making them particularly useful for studying hydrocarbon interactions in crude oil systems (Dong et al., 2022; Sedghi et al., 2016; Seyyedattar et al., 2019; Uddin et al., 2016). Despite the potential of MD simulations, few studies have thoroughly investigated the molecular interactions between wax crystals and polymeric inhibitors in crude oil systems. Most research has focused on characterizing wax crystal growth or the broad molecular composition of crude oil under various conditions (Letoffe et al., 1995; Musser and Kilpatrick, 1998). For instance, Gan et al. used MD simulations to explore *n*-alkane behavior during wax formation, providing early-stage insights into wax crystallization (Gan et al., 2019). However, there is a need to build on such work by delving deeper into how inhibitors interact with wax at the molecular level.

Several notable studies have laid the groundwork in this area. Duffy and Rodger (2000) investigated the interaction between acrylate inhibitors and Octacosane crystals using the CHARMM force field (Duffy and Rodger, 2000; Zhu et al., 2012). They found that acrylate dimers created inhibition by slipping into the crystal lattice with minimal disruption to the alkane structure. Zhang et al. (2004) used density functional theory (DFT) to study simplified systems and demonstrated that steric hindrance and electronegativity play a role in preventing wax deposition in diesel fuels. Wu et al. (2005) employed the CVFF95 force field to study the interaction of ethyl/vinyl acetate co-polymer variants with low molecular weight alkanes, concluding that the inhibitors disrupted crystal growth in the (001) plane surface while facilitating extension in the perpendicular planes. Similarly, while using a similar force field, Zhang et al. (2008) performed theoretical MD calculations on the (010) surface extracted from a C_{18} crystal unit. The study deduced that parallel orientation of the inhibitor onto the surface significantly inhibited crystal growth albeit, other surfaces were not investigated.

Notwithstanding these advances, the use of MD simulations to investigate more complex polymeric systems in crude oil using advanced force fields combined with precise modeling of molecules based on experimental data remains underexplored.

Advanced force fields like the COMPASS II force field have gained traction for their accuracy in representing such interactions, thanks to its comprehensive potential functions that accurately model both intra- and intermolecular forces (Sun et al., 1998, 2016). In this context, the COMPASS II forcefield offers distinct advantages over other force fields like CHARMM and CVFF95. While CHARMM is effective for biological molecules, “it is not optimized for polymer interactions due to its parameterization for aqueous environments and biomolecules” (Sun, 1998). Similarly, the CVFF95, though useful for small organic systems, this version of the force field lacks the precision needed for capturing the complex molecular interactions between hydrocarbons and polymers (Sun, 1998). In contrast, COMPASS II is more suitable for materials like hydrocarbons and polymers, offering a higher degree of accuracy in modeling non-bonded interactions such as van der Waals forces. Moreover, its inclusion of cross-term parameters allows for better simulation of interactions between wax molecules and polymer inhibitors, which is critical for accurately depicting the mechanisms of wax inhibition. The total energy, E_{total}, calculated using the COMPASS II forcefield is a summation of energy contributions from bonds (E_{bonds}), angles (E_{angles}), torsion ($E_{\text{dihedrals}}$), van der Waals and electrostatic energies (impropers), as well as cross-terms ($E_{\text{cross-terms}}$) that cater for energies due to angle-bonds and angle-torsions as shown in the following expression.

$$E_{\text{total}} = \sum_{\text{bonds}} E_{\text{bonds}} + \sum_{\text{angles}} E_{\text{angles}} + \sum_{\text{dihedrals}} E_{\text{torsion}} + \sum_{\text{impropers}} (E_{\text{vdW}} + E_{\text{electr}}) + \sum_{\text{cross-terms}} E_{\text{cross-terms}}$$

The cross-terms introduced in COMPASS II forcefield couple different types of bonded interactions between bond stretching, angle bending, and torsional motions, that are important for capturing the complexities in molecular systems.

Therefore, this study aims to address the gap in the current literature through the use of MD simulations with the COMPASS II force field and growth morphology algorithm to explore wax crystal growth behaviors, and interactions between polymeric inhibitors and crystal surfaces at a molecular level as well as devising an inhibition mechanism.

The structures of the wax and polymer molecule are obtained using Fourier transform infrared and protonated nuclear magnetic spectroscopy methods. The crude oil wax crystal data is obtained using X-ray diffraction. Through this molecular-level analysis, this research aims to contribute to a deeper understanding of how inhibitors function and the morphological transformation of wax crystals that could enhance flow assurance in the industry and reduce carbon footprint.

The remainder of this paper is organized as follows: the experimental section, which outlines the material/reagents, as well as laboratory and modeling methodologies used; the results and discussion section, which presents and analyzes the findings; and finally, the concluding remarks, which summarize the insights gained from the research.

2. Experimental section

2.1. Materials

The waxy oil used in this study was a surface sample provided by China National Petroleum Company from the Tarim basin, with properties presented in Table 1. The relative amounts of the oil's four components (SARA) were measured using FID-TLC gas chromatography; results are shown in Appendix A. The wax was extracted and its properties were determined in the laboratory.

The reagents used include *n*-heptane, *n*-hexane, calcined Alumina, petroleum ether, Dichloromethane, Trichloro methane, potassium bromide, Isopentyl alcohol, Toluene, xylene, Paraxylene, and Acetone supplied by Beijing Honghu United Chemical Products Co., LTD. Beijing Huatong Jingke Gas Chemical Co. Ltd supplied the helium gas.

The inhibitor is a synthesized copolymer variant of ethylene and vinyl acetate. The different compositions of an acetate/vinylic inhibitor were obtained. The structural makeup, composition, and efficacy were examined in the laboratory and the polymer with best efficacy was selected for molecular dynamic studies.

The molecular dynamic simulations were performed on a high-performance computer system with adequate processors and sufficient memory to handle the computational load.

2.2. Methodology

2.2.1. Wax extraction and wax amount

Wax extraction and determination of wax amount were done following the Chinese standard SY/T 7550–2000 (Yi and Zhang, 2011). The method is a step-by-step process that modifies the standard acetone method (Espada et al., 2010), as shown in Fig. 1.

Table 1
Reservoir and oil properties of the waxy oil.

Reservoir pressure, MPa	Reservoir temperature, °C	Density, g/cm^3 (20 °C)	Saturation pressure, MPa	Critical point, °C; MPa	GOR, m^3/m^3
37.57	111.0	0.8184	5.46	444.3; 7.92	243

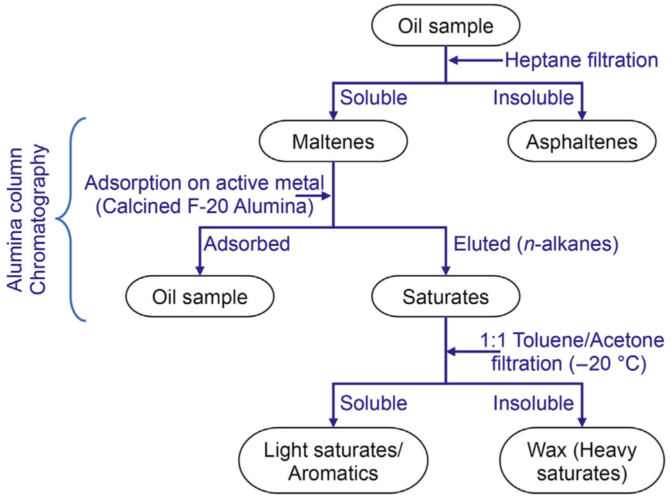

Fig. 1. A flowchart for the extraction and determination of wax content.

The oil sample was preheated and mixed with petroleum ether in a 1:30 (v/v) volume ratio, then poured down the calcined alumina-packed chromatographic column. Toluene was used as the eluant to wash down the oil wax. The eluate is collected in a weighed conical at a flow rate of 2 mL per minute. The flask was removed when an obvious black ring in the column reached the bottom section. Most excess solvent was evaporated in a hood before drying in a vacuum oven at 120 °C (25 kPa) for 60 min. The sample was mixed with 30 mL of dewaxing solvent (1:1 toluene/Acetone) and slowly heated in a water bath until the solution was transparent. The mixture was placed in a cold bath (−20 °C) for 30 min to allow complete wax precipitation. The precipitated wax was filtered using a vacuum pump at a constant rate of 1 drop per second. The filtrate (wax) was then dried for 5 min under vacuum.

2.2.2. *Wax appearance temperature (WAT)*

The viscosity method was used to determine the WAT point. The HAAKE MARS II rheometer was used with a cylindrical geometry measuring system. The experiment was conducted in open mode, and the oil's dynamic viscosity as a temperature function was measured. The parameters and experimental conditions under which the experiments were performed are given in Appendix C. The method is based on a principle that above the WAT, the crude oil behaves as a Newtonian fluid, a viscosity-temperature relationship modeled using the Arrhenius model, as shown in Eq. (1). However, when the wax crystals appear in the oil, the viscosity increases drastically with decreasing temperature, and the fluid behavior becomes non-Newtonian (Chhabra, 2010).

$$\mu = Ae^{\frac{E_a}{RT}} \tag{1}$$

where the activation energy, E_a, is typically 10–30 kJ/mol, and A is around $1\text{–}5 \times 10^{-3}$ Pa·s (Roenningsen et al., 1991).

2.2.3. *Gas chromatography*

The Gas chromatography experiment was conducted on the oil and extracted wax to identify the carbon number range (carbon distribution) of wax-forming saturates and their relative abundance in both samples. For the wax sample, 1 mg was put in a vial and dissolved in 1 mL of Dichloromethane. 1 μL of the sample was carefully drawn using a microliter syringe and rapidly inserted into the injector. The sample is also rapidly injected, after which the syringe is removed. The experiment column temperature was set to high temperatures (40–300 °C) at 20 °C/min. The peaks were analyzed using peak identification on a GC-MS instrument. A dilute sample was prepared for the oil sample by mixing two drops of the oil with 1 mL of Dichloromethane and then placing it into the vial. Before the sample placement, 2 mm of anhydrous sodium sulfate was placed at the bottom of the vial to remove all traces of water in the system. Then, 1 μL of the sample is injected into the column using a microliter syringe and rapidly eluted at the same temperature as the wax sample.

2.2.4. *Determination of inhibitor properties*

The inhibitor used in this study is an in-house synthesized variant of polyolefin and polyester copolymers. The molecular weight and degree of polymerization were determined using the viscosity method. The inhibitor viscosity is correlated to molecular weight using the Mark-Houwink-Sakurada (MHS) model that describes the intrinsic viscosity ($[\eta]$) of the dilute polymeric solutions and the molecular weight (M_v) of the inhibitor, as shown in Eq. (2) (Mai et al., 2023).

$$[\eta] = K(\overline{M_v})^{\alpha} \tag{2}$$

where K and α are constants.

A graph displaying this equation is presented in Appendix B and the determined inhibitor properties are presented in Table 2.

2.2.5. *Effect of polymeric inhibitor on the rheology of wax oil*

The inhibitor used in this study is an in-house synthesized copolymer variant of ethylene and vinyl acetate. Its efficacy was determined using the rheological method. Using the cylindrical geometry of the MARS HAAKE II rheometer, the inhibitor was injected into the oil sample at a temperature above the determined WAT point, and the apparent viscosity of the oil was measured as a function of temperature decrease.

2.2.6. *Molecular structural analysis*

The molecular structure of the wax and inhibitor was determined using Fourier transform infrared (FTIR) and proton nuclear magnetic resonance (H-NMR) spectroscopy methods. The former was used to determine functional groups in the samples, whereas the latter was used to determine the various chemical environments in the samples.

Table 2
Inhibitor properties.

Device parameters	Details
Glass transition temperature, T_g	−65 ± 1 °C
Molecular weight	4800 g·mol^{-1}
Degree of polymerization	421 units

To run the FTIR analysis of the wax and inhibitor samples, 200 mg of dried spectroscopic-grade potassium bromide (KBr) and 1 mg of each sample were weighed and placed in a stainless steel capsule containing ball bearing. The capsule was shaken on a Wig-L-Bug device for 2 min. Then, the sample was evenly distributed over the surface of a stainless steel disc and compressed under a vacuum using a hydraulic press at a pressure of 16000 psi for 6 min. A transparent thin disc layer containing the inhibitor sample and KBr is made and carefully removed and placed in the spectrometer cell holder to run the test. The test parameters are shown in Appendix C.

For the H-NMR analysis, 10 mg of each sample was dissolved in 1.0 mL of Deuterochloroform ($CDCl_3$), containing a small percentage of the reference compound TMS, and added to the NMR tube using a Pasteur pipette. The pipette consists of a wad of glass wool to filter out the tiniest particles of dust and metal particles that can affect the resolution. A fine stream of pure nitrogen is bubbled through the sample for 1 min to dispel the oxygen. Using Tetramethyl silane (TMS) as the reference marker, the signal recorded has an assured accuracy of about ±1 Hz. The carbon and proton chemical shifts were measured relative to the sharp TMS peak (0.0 ppm). It is noted that since the chloroform $CDCl_3$ used in the experiment was not 100% pure, the peak at 7.27 ppm in the proton spectrum belongs to ordinary residual $CHCl_3$ (Yadav, 2004).

X-ray diffraction analysis was used to obtain the crystal lattice parameters used in modeling the wax crystal in molecular dynamics. The extracted wax sample was crushed to a fine powder (<45 μm) and compressed into a pellet. The pellet was placed into the sample holder of the calibrated Bruker D8 Advance XRD equipment ($\lambda = 1.54598$ Å), and a diffractogram was obtained.

Molecular dynamics (MD) simulations were then conducted to model the interactions between the wax crystals and the polymeric inhibitor at a molecular level. The simulations were performed using the Materials Studio© software suite.

2.2.7. Molecular dynamics simulations

The methodology for modeling wax crystals and polymeric inhibitors and conducting molecular dynamics simulations to analyze molecular interactions was conducted as described in the following sections.

2.2.7.1. Modeling of wax motif and crystal. The wax motif was constructed using data from gas chromatography, FTIR, and H-NMR analyses. The molecular structure was optimized using the COMPASS II force field with a convergence tolerance of 1.0×10^{-4} kcal/mol to accurately model intermolecular forces. Vibrational energy and frequencies were calculated using Density Functional Theory (DFT) (Yang et al., 2020), and the simulated infrared spectra were compared with experimental FTIR data for validation.

The wax crystal lattice was modeled using X-ray diffraction (XRD) data. Noise in the diffractogram was removed, and cell parameters were refined using the Pawley refinement method (Pawley, 1981) and fitted to experimental data with the pseudo-Voigt function (David, 1986). Morphology modeling calculations were performed to study crystal growth behavior using the Growth Morphology algorithm. Attachment energy (E_{att}) for various crystal faces was calculated using Eq. (3):

$$E_{att} = E_{slice} - E_{latt} \tag{3}$$

where E_{slice} is the energy of the wax growth surface with thickness d_{hkl}, and E_{latt} is the lattice energy of the wax crystal. Attachment energy was used to predict the relative growth rates of crystal facets.

This method assumes that a crystal surface's growth rate is proportional to its surface potential energy. This potential energy can also be defined as attachment energy, which is the energy that is released when a species is adsorbed on a growing crystal face in a vacuum system. (Berkovitch-Yellin, 1985; Docherty et al., 1991).

2.2.7.2. Modeling of polymeric inhibitor. The polymeric inhibitor was modeled as a block copolymer with a 3:2 ratio of ethylene to vinyl acetate units, as determined through experimental rheology measurements (Appendix E). Chemical characterization of the copolymer was conducted using FTIR, H-NMR, viscometry, and Mark-Houwink-Sakurada analysis. The structure was optimized using the COMPASS II force field with a convergence tolerance of 1.0×10^{-4} kcal/mol. Conformers of the polymer were generated, and the most stable conformer with the lowest ground state energy was selected using the Boltzmann jump method and the Metropolis selection criterion. This optimized polymer structure was used in MD simulations to evaluate interactions with wax crystals.

2.2.7.3. Structural validations, crystal growth, and adsorption MD simulations. Simulations were conducted to analyze molecular mobility, inhibitor efficacy in preventing crystal growth, and the structural behavior of wax crystals.

The molecular structures of the wax and polymer were validated by comparing their simulated infrared spectra with experimental FTIR data. Vibrational analysis, based on the Hessian matrix and Born effective charges, was used to calculate vibrational frequencies and intensities, ensuring that the modeled structures accurately represented the physical and chemical properties of the materials.

The wax motif consisted of C_{28} alkanes arranged in a rhombohedral pattern, forming a lattice with four molecules per unit cell. The C_{28} alkane molecule and lattice were optimized using the COMPASS II force field with a convergence tolerance of 1.0×10^{-4} kcal/mol to achieve its ground state energy. The Wax crystal growth was simulated using the Morphology module of the Materials Studio package. The fastest growing crystal facets were identified, and their attachment energies were calculated. A cleaved slab of the fastest facet was prepared, with a vacuum space of 20 Å created above it to accommodate the polymer inhibitor.

Using the Adsorption Locator tool, the cleaved crystal slab was loaded with the polymer inhibitor. Low-energy adsorption sites (preferential binding sites) were identified using the simulated annealing algorithm, and adsorption energy was calculated to quantify the interaction between the polymer and the wax crystal surface.

3. Results and discussion

3.1. Wax appearance temperature (WAT)

Using the viscosity method and based on the fact that oil ceases to exist as a Newtonian fluid once the wax starts to form in the oil, the WAT point was determined to be at about 34.3 °C (Fig. 2). At this point, the oil's viscosity deviates from Newtonian behavior that conforms with the Arrhenius model. This is indicative of the wax appearance in the oil sample as temperature decreases.

3.2. Carbon number distribution

The length, *l*, of the molecule (wax) is related to the carbon number, *n*, as suggested in the generalized molecular formula for saturates, C_nH_{2n+2}. The gas chromatography experiment results for the oil and wax revealed that the oil sample has a carbon composition range from C_1 to C_{40}. The pure wax sample has a carbon composition range between C_{15}–C_{40} (Fig. 3). This wax composition implies that the alkanes with a carbon number greater than 14 are the wax

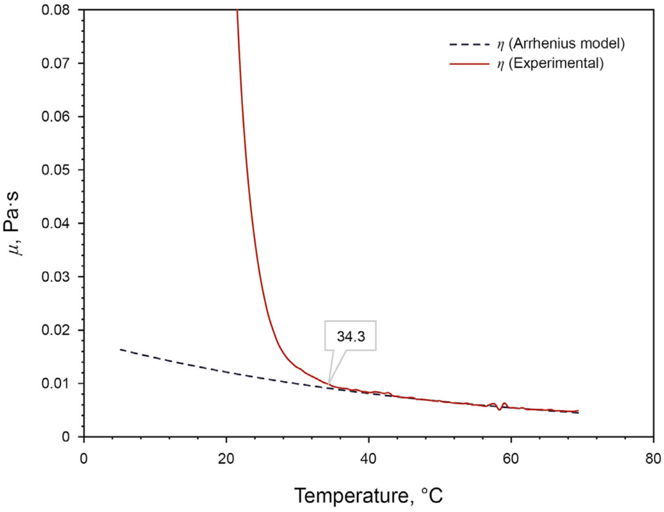

Fig. 2. Wax appearance temperature of the waxy oil.

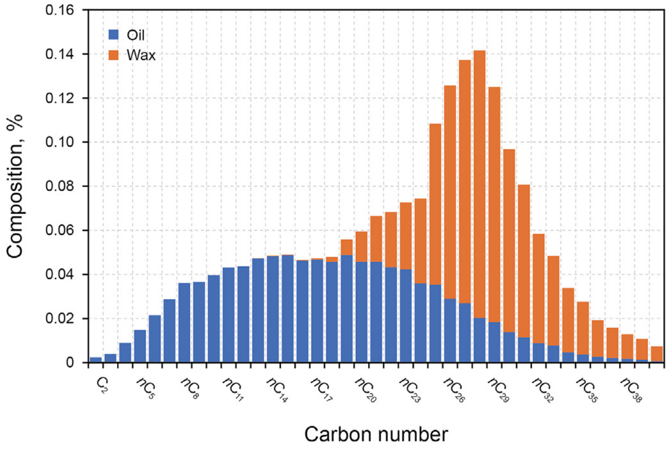

Fig. 3. GC analysis for carbon number distribution of oil and wax samples. The oil composition is between C_1 and C_{40}, and the wax is mostly between C_{15} and C_{40}.

forming species. Among these species, the majority composition in the wax ranges from C_{25} to C_{34}. Due to the robust nature of molecular calculations and resource intensiveness, it is impossible to simulate the entire range of molecules, especially for complex fluids like oil; thus, for this study's purpose, the component that makes up the highest percentage was considered and, in this case, its C_{28} where $n = 28$. According to the general molecular for alkanes, the wax molecule used as the motif has a chemical formula $C_{28}H_{58}$.

The selection of C_{28} as the representative species for modeling the wax motif is based on the results in Fig. 3, which show alkanes in the C_{25}–C_{34} range as the dominant wax forming species in the sample of which C_{28} was the most abundant. Given the computational challenges of modeling the entire range of molecules in a complex fluid like crude oil, C_{28} was chosen as a balance between accuracy and computational feasibility. While heavier hydrocarbons ($C > 40$) are known to exist in crude oils, their contribution to the wax crystallization process under the studied conditions is minimal due to their lower concentrations and higher melting points. Thus, the chosen model adequately captures the primary mechanisms of wax formation and interaction with inhibitors, as validated by experimental XRD data and the close match between the simulated and experimental lattice structures.

3.3. Wax and inhibitor spectral analysis

3.3.1. Wax spectral analysis

From the FTIR spectrum shown in Fig. 4(a), the principal absorption peaks are observed at wavenumbers 2915.84, 2847.38, 1463.22, 1377.89, and 720.28 cm^{-1} in that order respectively.

Compared with theoretical values, a detailed spectral analysis is presented in Table 3 to illustrate the functional groups that constitute the wax structure in question.

The bending symmetrical bond with wavenumber 1377.89 cm^{-1} is characteristic of straight-chain alkanes, whereas the rocking vibration at 720.28 cm^{-1} is unique for the $(CH_2)_n$ for which n is greater than 4. Moreover, the absence of three bands and two bands in the wavenumber range (2840–3040 cm^{-1}) eliminates the possibility of cycloalkanes. Therefore, with certainty, the main groups in the wax sample are CH_3 and CH_2. Although not conclusive, it can be deduced that the molecule is of the structure $CH_3{-}(CH_2)_{26}{-}CH_3$. Nonetheless, an NMR spectral analysis was done to confirm the chemical environments.

The H-NMR spectral intensity peaks in Fig. 4(b) appear at 0.0002, 0.8682,0.8801, 0.8914,1.2550, and 7.2573 ppm chemical shifts. The peaks at 0.0002 ppm and 7.2573 ppm are insignificant in the structural analysis as they belong to the standard used (TMS) and contamination from Deuterium Chloride ($CDCl_3$) solvent, respectively. The triplet with chemical shifts at 0.8682, 0.8801, and 0.8914 ppm is characteristic of a $-CH_3$ chemical environment, whereas the singlet with a chemical shift of 1.2550 ppm is from a methylene group ($-CH_2-$). Moreover, of significant importance in this spectrum is the integrated area results that show the methylene occupying an area of 6.61 mm, six times that occupied by the terminal methyl groups (1.00 mm). It is also crucial to the lack of peaks downfield, which implies the absence of carbonyls, aromatics, and unsaturated species.

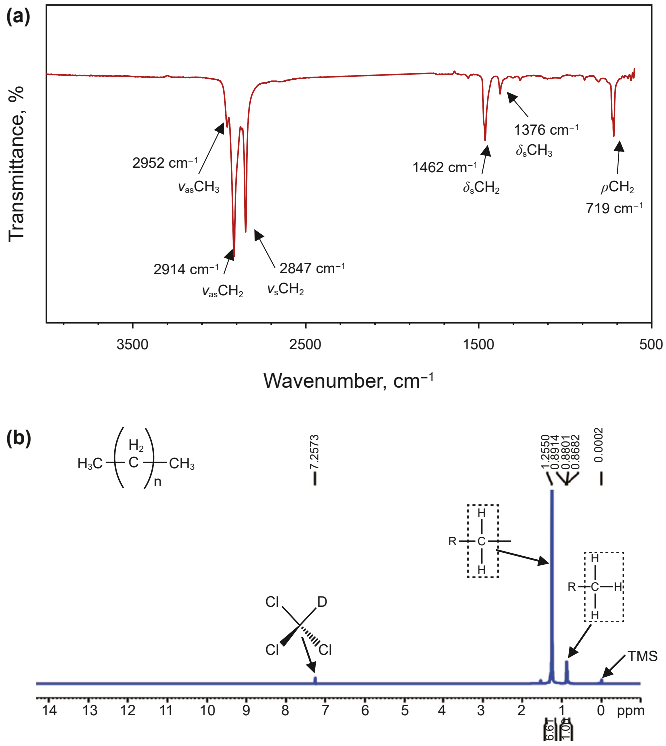

Fig. 4. Spectral analysis of the wax. **(a)** FTIR spectrum; **(b)** H-NMR spectrum.

Table 3
Analysis of FTIR spectrum for wax sample.

Bond Type	Functional group	Wavenumber, cm^{-1}	Bond symmetry
C–H stretching (νC–H)	$-CH_3$	2952.97	$\nu_{as}CH_3$
	CH_2	2847.38	$\nu_{s}CH_3$
		2915.84	$\nu_{as}CH_2$
C–H bending (δC–H)	CH_3 and CH_2	1463.22	$\delta_{as}CH_3$ and CH_2
		1377.89	$\delta_{s}CH_3$
CH_2 rocking ρCH_2	CH_2	720.28	ρCH_2

Since it is clear that there are no chemical shifts of protons from secondary carbon (R_2CH_2), usually with a chemical shift of 1.3 ppm, nor a chemical shift from a tertiary environment (R_3CH) that is generally reported at about 1.5 ppm, it implies that the molecule has a straight linear structure.

3.3.2. Inhibitor spectral analysis

FTIR analysis of the inhibitor shows that the most significant absorption peaks are observed at wavenumbers 2850.24–2917.59, 1234.95, 1732.32, and 719.24 cm^{-1} in that order, respectively, as can be observed from the spectrum presented in Fig. 5(a).

The stretching vibrating bonds whose absorption occurs in the range 2850.24–2918.59 cm^{-1} belong to the symmetrical and asymmetrical saturated C–H bond. Similarly, the rocking vibration band observed at the 719 cm^{-1} peak indicates the absorptions from methylene groups $(CH_2)_n$ greater than four. Peaks in the range 1820–1625 cm^{-1} belong to a carbonyl group (Badertscher et al., 2009; Pouchert, 1997). Therefore, due to the observed strong carbonyl peak at 1734.32 cm^{-1} and the strong, broad single ester-carbonyl peak in 1310–1100 cm^{-1} (1234.95 cm^{-1}) range, it is deduced that there is the existence of a conjugated ester. The functional groups from which the chemical structure of the inhibitor can be qualitatively analyzed include saturated C–H, $(CH_2)_n$ ($n > 4$), and ester groups.

From the H-NMR spectrum (Fig. 5(b)) of the polymeric inhibitor, the peaks upfield have spectral intensity peaks at 0.0002, 1.2512, 1.4971, 2.0187, and 2.0340 ppm, while those downfield are seen at peak values 4.8410, 4.8513, 4.8609, and 7.2611 ppm. The peaks at 0.0002 and 7.2573 ppm belong to the standard used (TMS) and the solvent Deuterium Chloride ($CDCl_3$), respectively. Moreover, the chemical shifts at 1.2512 ppm and 1.4971 ppm are structural characteristics of environments with methylene protons ($-CH_2-$), while the peaks at 2.0187 and 2.0340 ppm shifts are associated with methyl protons ($-CH_3$) in the ester group. The chemical shifts in the spectrum region 4.8410–4.8609 ppm correspond to methine protons (–CH) plausibly in a vinylic acetate structure of the inhibitor (Yang, 2018). From the integrated values for the methyl and methine protons are 1.00 and 0.34 respectively, confirming an expected 3:1 proton ratio between the methyl and methine groups in a vinyl acetate unit. Similarly, the integration values, 1.24 and 5.37 for the methylene group indicate significant proton contributions from an ethylene structure. Thus, it is deduced that the inhibitor compound is a copolymer of an olefin and an ester. From the analysis of the integrated values, a relative ratio of 4:1 of the ethylene olefin to vinyl acetate ester was calculated, implying four ethylene units for every vinyl acetate unit hence a higher ethylene content in the inhibitor.

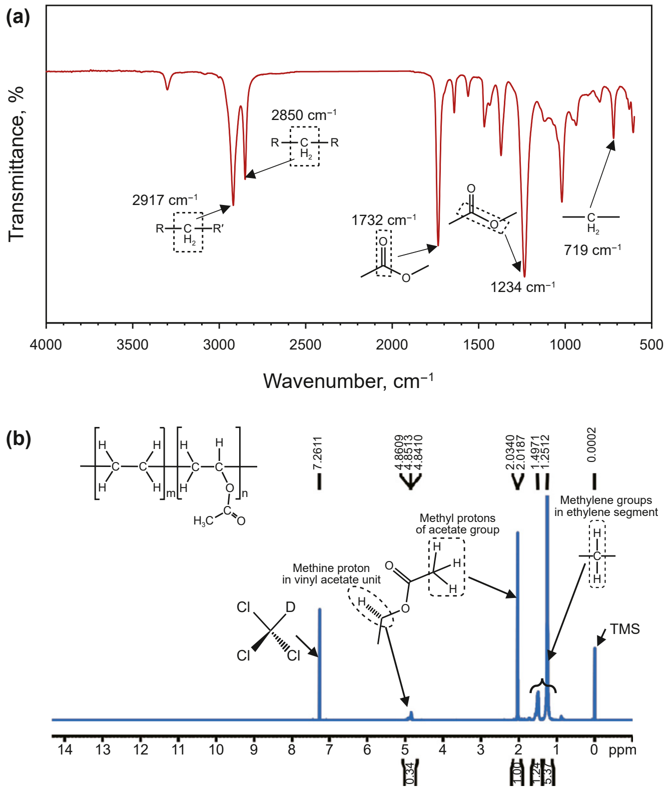

Fig. 5. Spectral analysis of the inhibitor. **(a)** FTIR spectrum, **(b)** H-NMR spectrum.

3.4. Effect of polymeric inhibitor on the rheology of wax oil

As observed in Fig. 6, the inhibitor effectively shifts the WAT to lower temperatures (34 to about 25 °C). Similarly, a 500 ppm

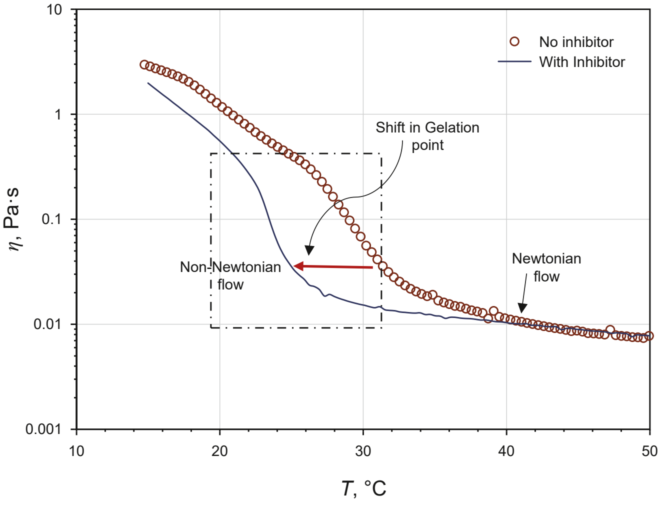

Fig. 6. Inhibitor effect on the WAT and viscosity in waxy oil. Flow in the non-Newtonian phase is significantly improved.

inhibitor dosage to the waxy oil sample significantly improves the oil fluidity, as indicated by the arrow. This shift in the gelation region implies that the inhibitor disrupts the wax's crystalline network, hindering aggregation and growth. This phenomenon likely leads to smaller wax crystals or a more dispersed distribution, contributing to lower oil viscosity. Although unexpected, the reduction in WAT point suggests the inhibitor possibly affects the nucleation rate or provides a barrier to crystal growth that may be attributed to the likely response between the hydrogen moieties of the wax molecules and the highly concentrated HCOOR functional groups present in the inhibitor.

Therefore, these results underscore the efficacy of the polymeric inhibitor in remediating wax-related challenges in oil production and transport that warrants a molecular-level investigation to decipher the intricate mechanisms behind this phenomenon.

3.5. Molecular dynamics and mechanism of inhibition

3.5.1. Wax molecule and inhibitor models

After determining the suitable conformer to the inhibitor, the structures of both molecules were optimized, and the results are shown in Fig. 7. For both structures, the energy sharply decreases away from high energy configurations towards a more stable configuration. After the sharp drop, both energy profiles level off, indicating that the structures are at minimum energy (about −420 kcal/mol for the inhibitor and about −72 kcal/mol for the wax).

Using the density functional theory (DFT), the bond energies for both the wax and polymeric inhibitor molecular structures were calculated. With the calculated energies, a vibrational analysis of the molecules was done to ensure that the structures agree with the FTIR experimental data. From the comparative analysis of the computed frequencies with the experimental data, we observed similarities in peak distributions for the functional groups constituting both modeled molecules and the experimental samples. In Fig. 8, comparisons are made between the simulated and experimental infrared spectra of the wax and inhibitor, demonstrating the alignment in peak distribution and molecular features between the two. Although, there are evident differences in the intensity, number, and positions of distinctive peaks, the main peaks in the simulations are closely correlated with the experimental peaks observed. These variations observed arise from inherent limitations in both computational and experimental methods.

In computational vibrational analysis, IR absorption intensities are calculated using the Hessian matrix and Born effective charges. The Hessian matrix determines vibrational frequencies, while the Born charges quantify dipole moment changes during molecular vibrations.

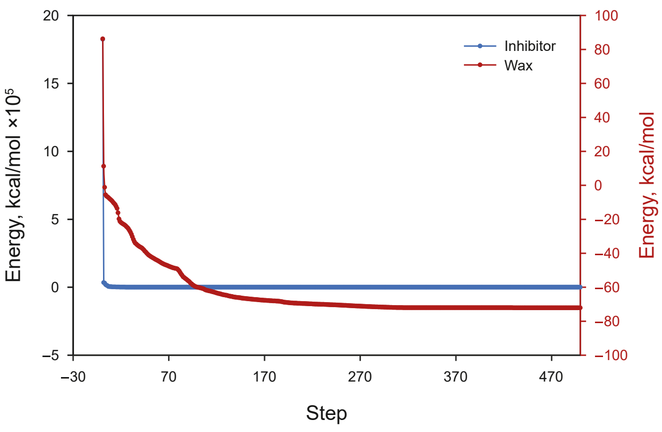

Fig. 7. Wax and inhibitor geometry optimisation.

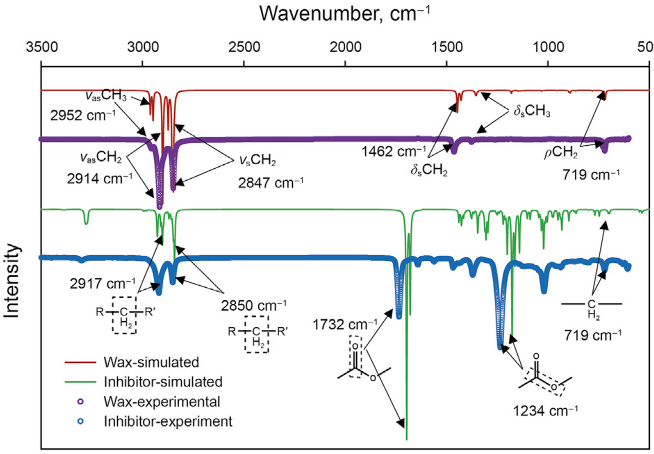

Fig. 8. Comparative analysis of modeled structures vibration frequencies with experimental frequencies. A close match between experiment and simulated bond vibrations is observed for wax and inhibitor molecules.

However, these calculations rely on approximations such as the harmonic oscillator model, which assumes perfectly harmonic vibrations. In reality, molecular vibrations often exhibit anharmonic behavior, particularly for higher-energy or large-amplitude modes, leading to discrepancies in intensity. Experimental spectra, on the other hand, reflect additional complexities such as interactions with solvents, impurities, and environmental conditions, which influence peak intensities. Furthermore, instrumental factors like resolution, sensitivity, and noise can cause deviations. Despite these differences, the comparison demonstrates that the simulated spectra capture the key molecular arrangements and vibrational frequencies of the experimental structures, validating the modeled system.

3.5.2. Wax crystal structure

Crystalline structures are defined by motifs (asymmetric units), lattices, and space groups. The motif, comprising atoms, combines with the lattice—a mathematical construct describing a theoretically infinite array of points with identical environments in one, two, or three dimensions—to underpin crystal architecture. While ideal lattices are borderless, real crystals possess surfaces that exhibit distinct physical and chemical properties from their bulk (McPherson, 2011). The unit cell forms the lattice's foundation, with lattice points marking the juncture of adjacent cells and residing at each unit cell corner.

Motifs fill these unit cells, embodying the lattice points, which, through translational symmetry, replicate across the crystal. Consequently, all crystal building blocks adhere uniformly to this translational symmetry in the modeling process, rendering the lattices congruent. Space groups delineate the symmetry within crystalline materials, encompassing symmetry operations that transform the motif into the complete crystal structure.

Dorset (1997) performed comprehensive X-ray diffraction studies on different types of wax. The study remains a benchmark in the field, as it comprehensively analyzed wax crystals from diverse origins and identified a universal orthorhombic crystal system. In this study, we compared the crystal lattice parameters obtained from our simulations to those reported by Dorset to validate our model. This comparison focused on lattice edge parameters and symmetry, ensuring consistency with established experimental findings. While we acknowledge that newer studies may provide additional insights, no other work has matched the scope and depth of Dorset's analysis for wax crystal types from different sources.

Moreover, it was deduced that If the motif carbon number, *n*, is odd, the average structure packs in an **A2$_1$am** space group, but in this case, because the component making up the majority of the wax has an even carbon number, 28, then the structure packs in a **PCa2$_1$** space group to form a crystal lattice as shown in Fig. 9(a)–(c).

The background from the raw X-ray diffraction data of the wax sample was calculated and subtracted from the raw experimental data to remove the noise diffractogram. The denoised XRD data was refined using the Pawley method and the Pseudo-Voight function. A good match between the simulated wax lattice and experiment XRD was obtained upon the Pawley refinement calculations. This implies that the refinement accurately models the wax lattice structure as an Orthorhombic type with **PCa2$_1$** space group. As displayed in Fig. 10, the model's peak positions align well with the experimental data, with 9.26% Profile *R*-factor (R_p) and 15.58% weighted Profile *R*-factor (R_{wp}). These fitness values suggest a reasonably good fit between the model and experimental data, indicating that the MD simulations accurately captured the crystallography of the wax.

Moreover, a comparison between Dorset's (1997) lattice edges for an even carbon number wax and the simulated model shows that lattice model edge parameters *a*, *b*, and *c* are in close agreement with Dorset's finding, as shown in Fig. 11.

3.5.3. *Wax crystal growth and morphology*

Using the Donnay-Harker prediction method, the growth morphology algorithm calculates the attachment energy of stable surfaces (hkl) on the wax crystal. As shown in Fig. 12 and in Appendix F, the arrows highlight the fastest-growing planes, while the predicted morphology reveals dominant growth in the X and Y directions. The computed energy is then used to determine the morphology of the crystal using the Wulff method (Bentivoglio, 1927; Donnay and Harker, 1937; Wulff, 1901). A crystal habit is generated with an aspect ratio of 15.434 and a relative surface-to-volume ratio of 2.507 (Fig. 12). This aspect ratio reflects the plate-like crystal morphology as it grows, diminishing the needle-like nature morphology.

Ten (10) facets are generated, of which only five (5) are systemically unique (Table 4). These facets were deduced in the experimental XRD analysis (Fig. 9). The (002) face is the slowest growing face, accounting for a total area of more than 80%. Analysis of the center-to-plane distance suggests that the faces (010) and (110) are the fastest-growing, with the latter being the fastest of all faces. These faces are represented as arrows in Fig. 13, normal to the growth planes (with their bases on the planes).

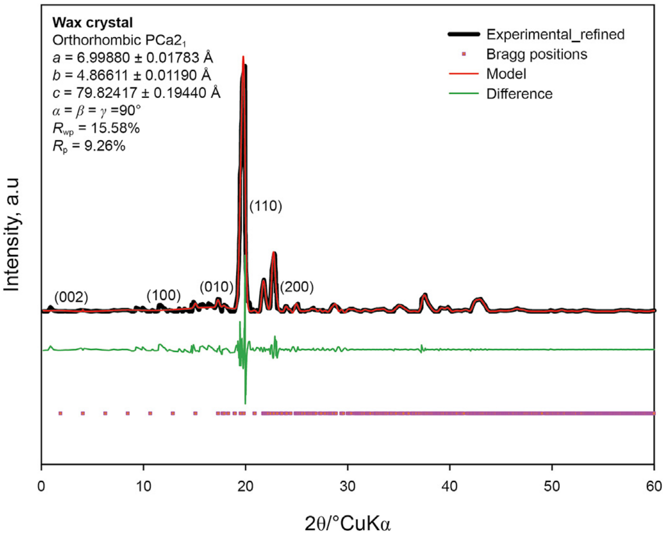

Fig. 10. Overlay of experimental and calculated XRD for the wax lattice. The Pawley refinement method obtained a 9.26% Profile *R*-factor (R_p) and 15.58% weighted Profile *R*-factor (R_{wp}).

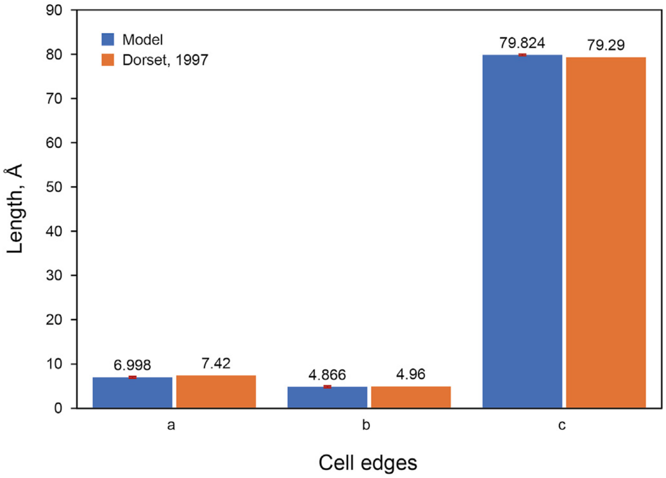

Fig. 11. Comparison between Dorset lattice edges and the simulated model.

Therefore, it is only plausible that an effective inhibition of wax growth in oil requires an inhibitor that effectively blocks the growth of these faces or at least one. The surface (110) was cleaved

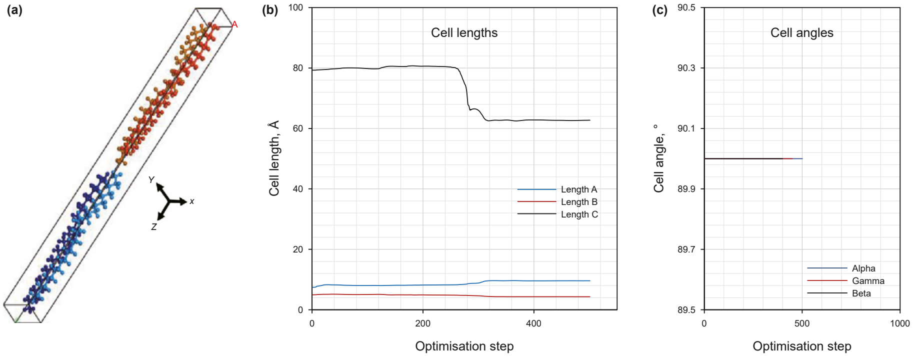

Fig. 9. (**a**) Wax crystal lattice; (**b**) Optimized lattice cell length; (**c**) Optimized lattices angle parameters.

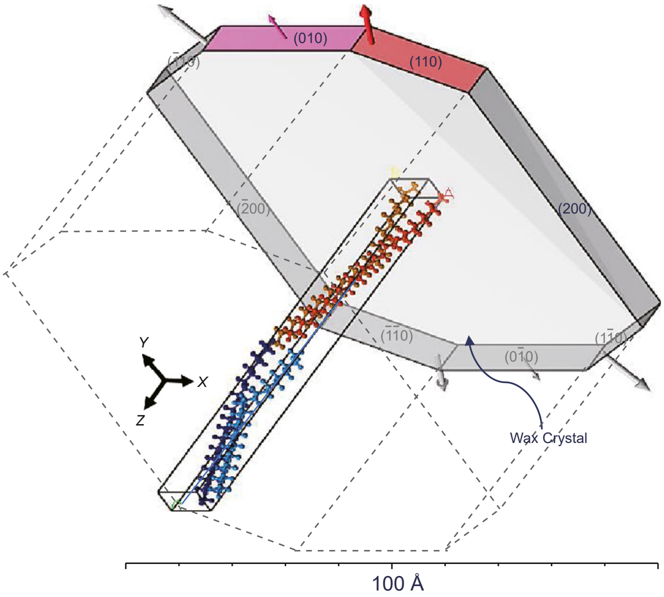

Fig. 12. Calculated wax crystal Habit. On the habit diagram, symmetrically unique facets are displayed.

out of the crystal, and interactions between this surface and the inhibitor were analyzed to determine the possibility of adsorption onto the surface by calculating the binding energies. For the inhibitor to adsorb onto the crystal surface and block its growth, its adsorption energy must be greater than the attachment energy of the (110) surface. Using the COMPASS II forcefield and the Monte Carlo theory, the plausible adsorption sites were identified and ranked based on the energies for each generated configuration.

The calculated energies for the first-ranked configuration are given in Table 5. Calculated absorption energy is a sum of the inhibitor's deformation and rigid adsorption energies. Respectively, these energies are due to the relaxation of the inhibitor and its adsorption onto the wax crystal surface. The differential energy is the energy required to detach the inhibitor from the surface.

Through the calculations, it was determined that the attachment energies for the (010) and (110) surfaces were −144.09 and −180.25 kcal/mol respectively.

3.5.4. *Inhibition mechanism*

Since the adsorption energy is more negative than the attachment energy of the fastest-growing faces, it is deduced that the inhibitor effectively adsorbs onto the surface (110) thereby inhibiting the growth of the wax crystal. This phenomenon limits the size of the wax crystals to one with a low aspect ratio and limits the probability of contact between wax crystals, hence low viscosity. Moreover, the ethylene groups that are repelled away from the wax surface successively repel away other non-polar groups from inhibitor segments attached to other wax molecules limiting aggregation and lowering the viscosity of waxy oils. This interaction mechanism between the wax surface and the polymeric inhibitor during the inhibition process is illustrated in Fig. 13.

A low olefin composition yields better inhibition and a high composition gives a low improvement in fluidity as shown in Appendix E. The high effect is attributed to the response between the hydrogen moieties of the wax molecules and the highly concentrated HCOOR functional groups in the inhibitor. A high olefin content creates a high density of hydrogen moieties thus wax molecules tend to repel the olefin hydrogens hence low performance.

While this study focuses on the molecular mechanisms of wax crystallization and inhibitor interactions, it is important to acknowledge the potential role of heavier hydrocarbons (C > 40) in influencing the macroscopic properties of crude oil, such as viscosity and gel strength. These components, though present in lower concentrations, may contribute to the overall rheological behavior of the system under different operational conditions. Future studies could explore the integration of these heavier hydrocarbons into

Table 4
Miller indices and energy of symmetrically unique facets.

	hkl	Multiplicity	Distance, Å	Area, Å^2	d_{hkl}, Å	$^aE_{att}$(total), kcal/mol
1	{0 0 2}	1	11.32	7.41 × 10^4	35.36	−11.32
2	{0 0 $\bar{2}$}	1	11.32	7.41 × 10^4	35.36	−11.32
3	{2 0 0}	2	138.411	4.80 × 10^3	4.20	−138.41
4	{0 1 0}	2	144.095	2.88 × 10^3	4.27	−144.09
5	{1 1 0}	4	157.245	1.90 × 10^3	3.81	−157.25

[a] E_{att} is total attachment energy from van der Waal and electrostatic forces.

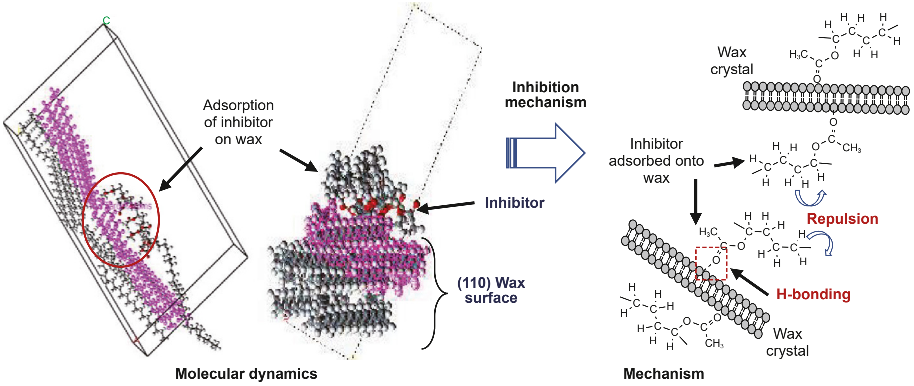

Fig. 13. Adsorption of the inhibitor on the crystal surface.

Table 5
Calculated energies.

Rigid adsorption energy, kcal/mol	Deformation energy, kcal/mol	Differential energy, kcal/mol	Adsorption energy, kcal/mol
−171.058	−9.187	−180.245	−180.245

molecular simulations to assess their indirect effects on wax nucleation and growth dynamics. However, their limited role in the dominant crystalline structure studied here ensures that the primary objectives of this research are not compromised.

4. Conclusion

This research harnesses molecular dynamics simulations to decipher molecular-level morphology, interactions, and inhibition mechanisms of wax in crude oil with polymeric inhibitors using the COMPASS II forcefield, hence bridging a critical knowledge gap. The main findings of this research are summarized as follows:

1) The wax composition was determined through GC analysis and found to be mainly composed of C_{28} alkanes. The molecular structures of the wax and inhibitor were characterized through the use of FTIR, XRD, and HNMR spectroscopy. The wax examined was mostly straight-chain normal alkane whereas the inhibitor was a co-polymer of ethylene and vinyl acetate.
2) The modeled molecular structures can be validated through a comparison of bond vibrational analysis and experimental FTIR data that gave favorable peak alignments. Similarly, the crystal structure of wax was validated through a replication of XRD data yielding a 9.26% Profile *R*-factor and 15.58% weighted Profile *R*-factor.
3) In agreement with XRD analysis, the COMPASS force field and the growth morphology algorithm used to model the wax crystal behavior revealed that ten (10) facets can exist but only five (5) facets are systemically unique.
4) Contrary to the original findings, it has been determined that the crystal surface (110) is the fastest-growing face emanating from the primitive rhombohedral crystal cell unit of the wax. An effective crystal growth inhibitor is required to have an adsorption energy of more than −150 kcal/mol to disrupt further expansion.
5) Through further analysis of interactions between the crystal surface and inhibitor, a mechanism is deduced that as the inhibitor molecules adsorb onto the wax surface, the non-polar groups face away from the surface and repel any similar approaching group. This repulsion effectively prevents aggregation of the wax crystals. This phenomenon explains the gelation flow behavior when inhibitors are applied to waxy crude oil.

Thus, in conclusion, the study confirmed that adding a specific inhibitor targeting specific sites on the crystal system in a colloidal system could dramatically disrupt the aggregation behavior of wax crystals in a fluid system which lowers the viscosity of the overall fluid system. Future research will include a broader range of inhibitor and oil chemistries coupled with an assessment of their environmental ramifications to accelerate the refinement and the design of inhibitors tailored to specific operational conditions. Such undertakings will advance scientific knowledge and likely yield practical, effective, and sustainable solutions for the industry.

CRediT authorship contribution statement

Wyclif Kiyingi: Software, Investigation, Formal analysis, Conceptualization. **Ji-Xiang Guo:** Supervision, Project administration, Funding acquisition, Conceptualization. **Rui-Ying Xiong:** Writing – review & editing, Project administration, Investigation, Formal analysis. **Chen-Hao Gao:** Writing – review & editing, Investigation, Data curation, Conceptualization.

Declaration of competing interest

The authors declare that they have no known competing financial interests or personal relationships that could have appeared to influence the work reported in this paper.

Acknowledgment

The principal author is grateful to the China Sponsorship Council for the scholarship funding (2022GXZ006306). The authors would like to acknowledge contributions from colleagues and support from the Sinopec Company project (No. P23138) and the National Natural Science Foundation of China (No. 52174047). We also appreciate the editors and the anonymous reviewers for reviewing the manuscript.

Appendix A

Percentage SARA composition of oil samples.

Table A.1
Relative amount of the SARA oil components

Compositions	Amounts, %
Saturates	76.41
Aromatics	6.46
Resins	9.92
Asphaltenes	7.22
Wax amount	21.3

Appendix B

MHS model to determine Inhibitor Molecular weight and degree of polymerization

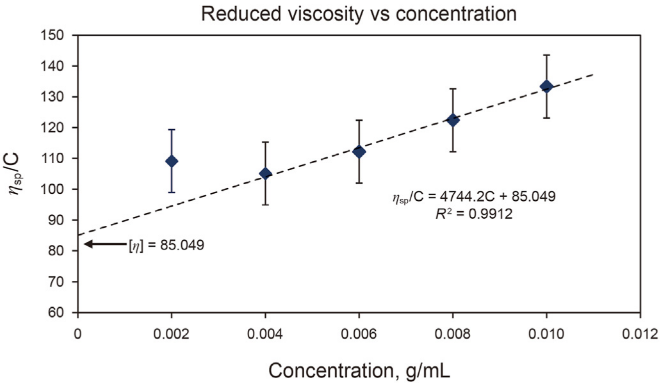

Fig. B.1. Reduced viscosity versus inhibitor concentration.

Appendix C. WAT testing parameters

Table C.1
Rheometer experimental parameters.

Device parameters	Details
Temperature device	MARS III Temperature Module
Measuring geometry	CC24 Ti
Cooling media	Water
a-factor	3.241×10^4 Pa/Nm
m-factor	8.668 (1/s)/(rad/s)
Inertia	3.074×10^{-6} kg m^2
Damping	30.00
Gap	5.000 mm
Experimental conditions	
Temperature range	70.00–10.00, °C
Shear rate, $\dot{\gamma}$	100.0, 1/s
Mode	Controlled rate, CR
Rotation	Rot T-Ramp
Cooling rate	0.003 °C/s or 0.2 °C/min

Appendix D

Table D.1
FT-IR test parameters.

Parameters	Details
Temperature	22 °C
Relative humidity	50%
IR-Scope	4000–400 cm^{-1}
Spectral resolution	4 cm^{-1}
Number of scans	32
Background scans	32
Sample gain	1.0

Appendix E

Rheological effect of the inhibitor visa viz composition and solvent concentration.

In both solvents (S-1 & S-2), the 40% acetate component inhibitor gives the best results, followed by 32%, 25%, 18%, and 12% samples, respectively. The gelation time is also increased, slowing down the solidification of the wax and the solvent concentration has no bearing on the performance of the inhibitor.

Appendix F

As shown in Fig. F.1, the arrows highlight the fastest-growing planes, while the predicted morphology reveals dominant growth in the X and Y directions.

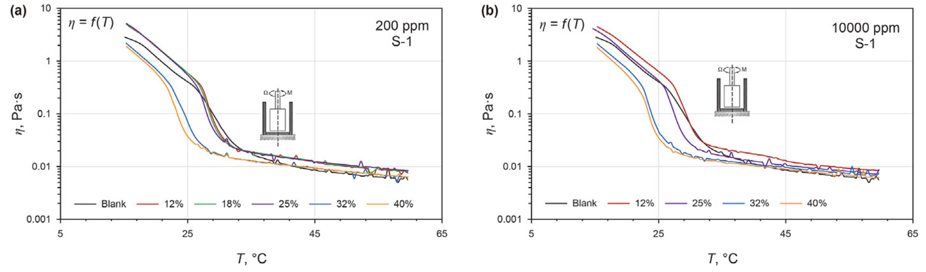

Fig. E.1. Inhibitor effect for different compositions in two solvent concentrations.

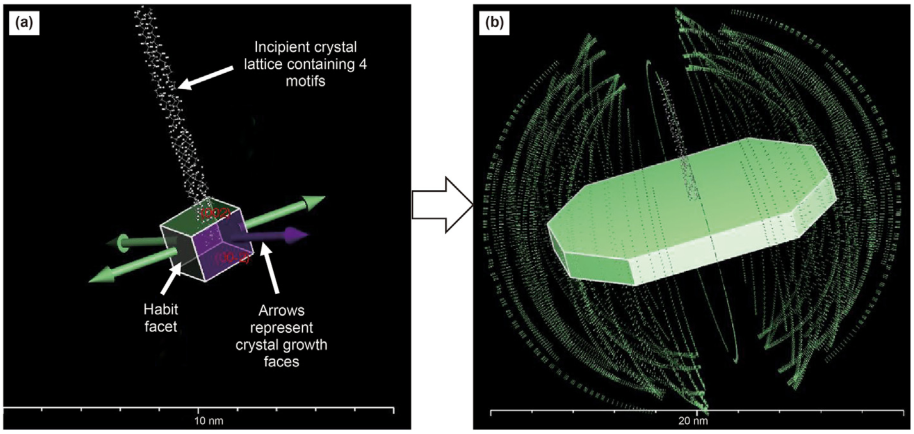

Fig. F.1. (**a**) Wax crystal lattice showing incipient motifs and habit facets. Arrows represent the growing crystal faces. (**b**) Predicted crystal morphology based on the Growth Morphology algorithm, with dominant growth in the X and Y directions forming a plate-like structure.

References

Badertscher, M., Bühlmann, P., Pretsch, E., 2009. Structure Determination of Organic Compounds: Tables of Spectral Data, fourth ed. Springer, Berlin, Heidelberg. https://doi.org/10.1007/978-3-540-93810-1.

Bentivoglio, M., 1927. An investigation of the rate of growth of crystals in different directions. Proc. R. Soc. Lond. - Ser. A Contain. Pap. a Math. Phys. Character 115 (770), 59–87.

Berkovitch-Yellin, Z., 1985. Toward an ab initio derivation of crystal morphology. J. Am. Chem. Soc. 107 (26), 8239–8253.

Chhabra, R.P., 2010. Non-Newtonian fluids: an introduction. In: Krishnan, J.M., Deshpande, A.P., Kumar, P.S. (Eds.), Rheology of Complex Fluids. Springer, New York, pp. 3–34. https://doi.org/10.1007/978-1-4419-6494-6_1.

David, W., 1986. Powder diffraction peak shapes. Parameterization of the pseudo-Voigt as a Voigt function. J. Appl. Crystallogr. 19 (1), 63–64. https://doi.org/10.1107/S0021889886089999.

Docherty, R., Clydesdale, G., Roberts, K., et al., 1991. Application of Bravais-Friedel-Donnay-Harker, attachment energy and Ising models to predicting and understanding the morphology of molecular crystals. J. Phys. Appl. Phys. 24 (2), 89. https://doi.org/10.1088/0022-3727/24/2/001.

Dong, X., Xu, W., Liu, et al., 2022. Insights into adsorption and diffusion behavior of shale oil in slit nanopores: a molecular dynamics simulation study. J. Mol. Liq. 359, 119322. https://doi.org/10.1016/j.molliq.2022.119322.

Donnay, J.D.H., Harker, D., 1937. A new law of crystal morphology extending the law of Bravais. Am. Mineral. 22 (5), 446–467.

Dorset, D.L., 1997. Crystallography of waxes-an electron diffraction study of refined and natural products. J. Phys. Appl. Phys. 30 (3), 451. https://doi.org/10.1088/0022-3727/30/3/018.

Duffy, D.M., Rodger, P.M., 2000. Modelling the interaction between the poly (octadecyl acrylate) inhibitor and an n-octacosane crystal. Phys. Chem. Chem. Phys. 2 (20), 4804–4811. https://doi.org/10.1039/B004812G.

Elkatory, M.R., Soliman, E.A., El Nemr, A., et al., 2022. Mitigation and remediation technologies of waxy crude oils' deposition within transportation pipelines: a review. Polymers 14 (16), 3231. https://doi.org/10.3390/polym14163231.

Espada, J.J., Coutinho, J.A., Pena, J.L., 2010. Evaluation of methods for the extraction and characterization of waxes from crude oils. Energy & Fuels 24 (3), 1837–1843. https://doi.org/10.1021/ef901378u.

Gan, Y., Cheng, Q., Wang, Z., et al., 2019. Molecular dynamics simulation of the microscopic mechanisms of the dissolution, diffusion and aggregation processes for waxy crystals in crude oil mixtures. J. Petrol. Sci. Eng. 179, 56–69. https://doi.org/10.1016/j.petrol.2019.04.059.

Haj-Shafiei, S., Workman, B., Trifkovic, M., et al., 2019. In-situ monitoring of paraffin wax crystal formation and growth. Cryst. Growth Des. 19 (5), 2830–2837. https://doi.org/10.1021/acs.cgd.9b00052.

Kiyingi, W., Guo, J.X., Xiong, R.Y., et al., 2022. Crude oil wax: a review on formation, experimentation, prediction, and remediation techniques. Pet. Sci. 19 (5), 2343–2357. https://doi.org/10.1016/j.petsci.2022.08.008.

Letoffe, J.M., Claudy, P., Kok, M.V., et al., 1995. Crude oils: characterization of waxes precipitated on cooling by DSC and thermomicroscopy. Fuel 74 (6), 810–817. https://doi.org/10.1016/0016-2361(94)00006-D.

Li, B., Guo, Z., Zheng, L., et al., 2023. A comprehensive review of wax deposition in crude oil systems: mechanisms, influencing factors, prediction and inhibition techniques. Fuel 357, 129676. https://doi.org/10.1016/j.fuel.2023.129676.

Li, N., Wu, W., Mao, G., 2021. Effect of modified ethylene vinyl acetate copolymers pour point depressants on flow properties of crude oil and corresponding mechanism analysis. Colloids Surf. A Physicochem. Eng. Asp. 630, 127602. https://doi.org/10.1016/j.colsurfa.2021.127602.

Mai, J., Garvey, C.J., Chan, C.M., et al., 2023. Synthesis and Characterisation of poly (3-hydroxybutyrate-co-3-hydroxyvalerate)(PHBV) multi-block copolymers comprising blocks of differing 3-hydroxyvalerate contents. Chem. Eng. J. 475, 146175. https://doi.org/10.1016/j.cej.2023.146175.

McPherson, A., 2011. Introduction to Macromolecular Crystallography, first ed. John Wiley & Sons. https://doi.org/10.1002/9780470391518.

Musser, B.J., Kilpatrick, P.K., 1998. Molecular characterization of wax isolated from a variety of crude oils. Energy & Fuels 12 (4), 715–725. https://doi.org/10.1021/ef970206u.

Paiva, F.L., Marchesini, F.V.H., Calado, V.N.M., et al., 2017. Wax precipitation temperature measurements revisited: the role of the degree of sample confinement. Energy & Fuels 31 (7), 6862–6875. https://doi.org/10.1021/acs.energyfuels.7b00812.

Pawley, G., 1981. Unit-cell refinement from powder diffraction scans. J. Appl. Crystallogr. 14 (6), 357–361. https://doi.org/10.1107/S0021889881009618.

Pouchert, C., 1997. The Aldrich Library of FT-IR Spectra. Aldrich Chemical Company, Milwaukee.

Roenningsen, H.P., Bjoerndal, B., Baltzer Hansen, A., et al., 1991. Wax precipitation from North Sea crude oils: 1. Crystallization and dissolution temperatures, and Newtonian and non-Newtonian flow properties. Energy Fuels 5 (6), 895–908.

Sedghi, M., Piri, M., Goual, L., 2016. Atomistic molecular dynamics simulations of crude oil/brine displacement in calcite mesopores. Langmuir 32 (14), 3375–3384. https://doi.org/10.1021/acs.langmuir.5b04713.

Seyyedattar, M., Zendehboudi, S., Butt, S., 2019. Molecular dynamics simulations in reservoir analysis of offshore petroleum reserves: a systematic review of theory and applications. Earth Sci. Rev. 192, 194–213. https://doi.org/10.1016/j.earscirev.2019.02.019.

Sun, H., 1998. COMPASS: an ab initio force-field optimized for condensed-phase applications overview with details on alkane and benzene compounds. J. Phys. Chem. B 102 (38), 7338–7364. https://doi.org/10.1021/jp980939v.

Sun, H., Jin, Z., Yang, C., et al., 2016. Compass II: extended coverage for polymer and drug-like molecule databases. J. Mol. Model. 22, 1–10. https://doi.org/10.1007/s00894-016-2909-0.

Sun, H., Ren, P., Fried, J., 1998. The COMPASS force field: parameterization and validation for phosphazenes. Comput. Theor. Polym. Sci. 8 (1–2), 229–246. https://doi.org/10.1016/S1089-3156(98)00042-7.

Taheri-Shakib, J., Shekarifard, A., Naderi, H., 2018. Characterization of the wax precipitation in Iranian crude oil based on Wax Appearance Temperature (WAT): Part 1. The influence of electromagnetic waves. J. Petrol. Sci. Eng. 161, 530–540. https://doi.org/10.1016/j.petrol.2017.12.012.

Uddin, M., Coombe, D., Ivory, J., 2016. Molecular dynamics analysis of compositional effects in hydrocarbon systems property calculations. Chem. Eng. J. 302, 503–515. https://doi.org/10.1016/j.cej.2016.05.080.

Van der Geest, C., Melchuna, A., Bizarre, L., et al., 2021. Critical review on wax deposition in single-phase flow. Fuel 293, 120358. https://doi.org/10.1016/j.fuel.2021.120358.

Wu, C., Zhang, J.L., Li, W., et al., 2005. Molecular dynamics simulation guiding the improvement of EVA-type pour point depressant. Fuel 84 (16), 2039–2047. https://doi.org/10.1016/j.fuel.2004.12.009.

Wulff, G., 1901. XXV . Growth and dissolution of crystal surfaces. Crystalline Materials 34 (1–6), 449–530. https://doi.org/10.1524/zkri.1901.34.1.449.

Yadav, L.D.S., 2004. Organic Spectroscopy, first ed. Springer Science & Business Media. https://doi.org/10.1007/978-1-4020-2575-4.

Yang, R., 2018. Analytical Methods for Polymer Characterization, first ed. CRC Press, Boca Raton. https://doi.org/10.1201/9781351213158.

Yang, D., Li, J., Luo, L., et al., 2020. Exceptional levofloxacin removal using biochar-derived porous carbon sheets: mechanisms and density-functional-theory calculation. Chem. Eng. J. 387, 124103. https://doi.org/10.1016/j.cej.2020.124103.

Yi, S., Zhang, J., 2011. Relationship between waxy crude oil composition and change in the morphology and structure of wax crystals induced by pour-point-depressant beneficiation. Energy & Fuels 25 (4), 1686–1696. https://doi.org/10.1021/ef200059p.

Zhang, J., Wu, C., Li, W., et al., 2004. DFT and MM calculation: the performance mechanism of pour point depressants study. Fuel 83 (3), 315–326. https://doi.org/10.1016/j.fuel.2003.08.010.

Zhang, J., Zhang, M., Wan, J., et al., 2008. Theoretical study of the prohibited mechanism for ethylene/vinyl acetate co-polymers to the wax crystal growth. J. Phys. Chem. B 112 (1), 36–43. https://doi.org/10.1021/jp073052k.

Zhu, X., Lopes, P.E., MacKerell Jr, A.D., 2012. Recent developments and applications of the CHARMM force fields. Wiley Interdiscip. Rev. Comput. Mol. Sci. 2 (1), 167–185. https://doi.org/10.1002/wcms.74.